Journal of Materials Chemistry A

PAPER

View Article Online
View Journal | View Issue

Cite this: *J. Mater. Chem. A*, 2014, **2**, 6198

Defect chemistry of Ti and Fe impurities and aggregates in Al_2O_3

Jessica K. Bristow, Davide Tiana, Stephen C. Parker and Aron Walsh*

Received 20th December 2013
Accepted 5th February 2014

DOI: 10.1039/c3ta15322c

www.rsc.org/MaterialsA

We report a theoretical evaluation of the properties of iron and titanium impurities in sapphire (corundum structured α-Al_2O_3). Calculations using analytical force fields have been performed on the defect structure with the metals present in isolated, co-doped and tri-cluster configurations. Crystal field parameters have been calculated with good agreement to available experimental data. When titanium and iron are present in neighbouring face and edge-sharing orientations, the overlap of the d-orbitals facilitates an intervalence charge transfer ($Fe^{III}/Ti^{III} \rightarrow Fe^{II}/Ti^{IV}$) with an associated optical excitation energy of 1.85 eV and 1.76 eV in the respective configurations. Electronic structure calculations based on density functional theory confirm that Fe^{III}/Ti^{III} is the ground-state configuration for the nearest-neighbour pairs, in contrast to the often considered Fe^{II}/Ti^{IV} pair. Homonuclear intervalence charge transfer energies between both Fe^{III}/Fe^{II} and Ti^{IV}/Ti^{III} species have also been calculated, with the energy lying in the infra-red region. Investigation of multiple tri-clusters of iron and titanium identified one stable configuration, Ti^{III}–(Ti^{IV}/Fe^{II}), with the energy of electron transfer remaining unchanged.

1 Introduction

The mineral corundum (α-Al_2O_3) is a transparent and mechanically tough material, widely used for industrial applications such as catalyst supports, substrate layers in photovoltaic devices and solid-state lasers.[1–3] The presence of metal impurities in α-Al_2O_3, predominantly iron and titanium, dramatically alters its optical properties. Previous studies concerning the defect structure of sapphire and other polymorphs of Al_2O_3 have been essential in understanding its optical properties and methods to optimise its functionality.[4–9] These studies, however, have not connected the multiple optical processes that occur within and between these cation impurities in a complete analysis.

Al_2O_3 formally consists of Al^{3+} and O^{2-} ions and adopts a trigonal lattice symmetry in its ground-state corundum structure.[10] The Al centres are surrounded by six oxide ligands in a distorted octahedral geometry filling 2/3 of all available octahedral holes. These octahedral units are linked in both face-sharing and edge-sharing orientations as parallel and perpendicular to the *c*-axis, respectively.[11] The relative orientation of the metal centres causes a pseudo Peierls distortion, resulting in neighbouring metal centres that are rotated at an angle of 64.3° away from each other. Elongation in pairs of the surrounding oxide ligands (Fig. 1) results in a pentagonal bipyramidal geometry belonging to the space group $R\bar{3}c$.[12] The tetrahedrally coordinated oxide ligands form a close-packed sub-lattice. The material is largely ionic in nature with a wide band gap of 9.25 eV.

To induce the colours characteristic of minerals formed from Al_2O_3 (*e.g.* blue sapphire and red ruby), the presence of impurities is required. As a consequence to doping, electronic energy

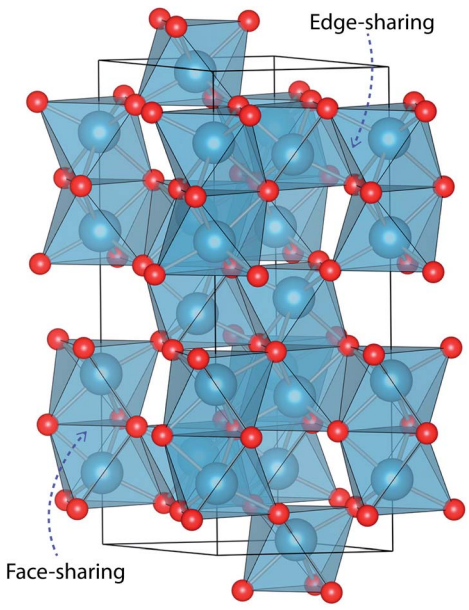

Fig. 1 Face-sharing and edge-sharing AlO_6 octahedral units in the corundum structure of Al_2O_3 (hexagonal crystal setting). The two sets of oxide ligands in the trigonal antiprismatic geometry (D_{3d} symmetry) are shown.

Centre for Sustainable Chemical Technologies and Department of Chemistry, University of Bath, Claverton Down, Bath, BA2 7AY, UK. E-mail: a.walsh@bath.ac.uk; Tel: +44 (0)1225 385432

levels are inserted into the band gap of the material. Lower energy transitions within the visible and/or thermal range can occur, giving rise to colour and conducting behaviour in the insulating and transparent host material.[13,14]

We have focused on two of the most common and researched impurities that increase the absorption of visible light. These impurities can be found in naturally occurring minerals or can be incorporated synthetically during synthesis or post-annealing. Titanium and iron, for electrostatic reasons, are primarily found in the trivalent state (Fe^{III}/Ti^{III}) at approximate concentrations ranging between 280 and 21 000 ppm.[15–17]

Titanium-doped sapphire is used in solid-state lasers.[18–20] The recognition that Ti^{III}, a d^1 cation, gives a tunable laser was reported in 1982.[21] It is the intra-valence d–d transitions occurring within the metal and the vibrational interactions with the sapphire lattice, which initiate the electronic transitions as a consequence of photon absorption. The interactions between the oxide host and titanium impurity are therefore crucial with regard to determining the optical properties of the doped material.[1,18] In addition to efficient emission of near IR (infrared) light, the ceramic material with a significant thermal conductivity also has a high damage threshold.[18,22]

Once present in the α-Al_2O_3 structure, Ti will substitute Al and remain on the same lattice site (eqn (1)). In addition to the isovalent Ti^{III} impurity, titanium has also been reported as Ti^{IV}. This tetravalent cation will cause a larger lattice distortion and therefore is found at lower concentrations in natural sapphire. Compensation mechanisms, such as those shown in eqn (2) and (3), are required for the aliovalent substitution in order to maintain overall charge neutrality. The binding energies between the isolated point defects and more complex charge compensating clusters have previously been calculated.[5,23]

The standard Kröger–Vink notation has been used to describe the charge compensation mechanisms, following the standard notation A_B^Y, where A represents the dopant, B the host lattice site and Y the charge relative to the host lattice site; $\times$ indicates no net charge. B can also be i, representing an interstitial defect and A can also be V, representing a vacancy defect.[24] Eqn (1)–(3) refer to reactions involving Ti^{III}, Ti^{IV} and Ti^{IV} respectively, with the atomic chemical potentials determined by the respective binary oxides.

$$Ti_2O_3 + 2Al_{Al}^{\times} \rightarrow 2Ti_{Al}^{\times} + Al_2O_3 \quad (1)$$

$$3TiO_2 + 4Al_{Al}^{\times} \rightarrow 3Ti_{Al}^{\bullet} + V_{Al}^{'''} + 2Al_2O_3 \quad (2)$$

$$2TiO_2 + 2Al_{Al}^{\times} \rightarrow 2Ti_{Al}^{\bullet} + O_i'' + Al_2O_3 \quad (3)$$

Iron-doped sapphire has not been as intensely studied as the Ti^{III}–Al_2O_3 system, but is still known to produce interesting optical properties. The increase in conductivity when doped with iron has applications including thin-film stress sensors and planar optical waveguides.[25] Sapphire doped only with iron has been shown to result in yellow crystals, demonstrating visible light absorption.[26] With homonuclear intervalence charge transfer and interactions with other dopants in the structure, iron-doped sapphire has the potential to display more complex optical properties. Again, two oxidation states can be incorporated, Fe^{II} (from FeO) and Fe^{III} (from Fe_2O_3):

$$Fe_2O_3 + 2Al_{Al}^{\times} \rightarrow 2Fe_{Al}^{\times} + Al_2O_3 \quad (4)$$

$$2FeO + 2Al_{Al}^{\times} \rightarrow 2Fe_{Al}' + V_O^{\bullet\bullet} + Al_2O_3 \quad (5)$$

$$3FeO + 2Al_{Al}^{\times} \rightarrow 3Fe_{Al}' + Al_i^{\bullet\bullet\bullet} + Al_2O_3 \quad (6)$$

Iron is present as Fe^{II} (eqn (5) and (6)) at a much lower concentration than Fe^{III} (eqn (4)); however, the concentration of divalent iron can be increased by the application of heat.[27] Lehmann and Harder (1970) gave an extensive review of the effect of the concentration of Fe^{III} and Fe^{II} on the colour of corundum crystals, also confirming in natural samples the isovalent Fe^{III} to be the dominant oxidation state.[28] The transfer of an electron between the two valence states of iron can also be initiated by light (eqn (7)). The energy required for the described homonuclear charge transfer between neighbouring Fe^{III} and Fe^{II} will be calculated and compared to the experimentally determined values ranging from 1.40–1.55 eV (800–886 nm).[26,29]

$$Fe_{Al}' + Fe_{Al}^{\times} \xrightarrow{h\nu} Fe_{Al}^{\times} + Fe_{Al}' \quad (7)$$

The substitution of both iron and titanium in Al_2O_3 results in the vibrant blue colour of sapphire crystals. The energy and intensity of light absorbed by the material has been shown to be dramatically affected by the concentration of either cation.[30,31] With multiple charge transfer and intra-valence excitations occurring between and within these cations, spectroscopic analysis of natural sapphire samples is often disputed and inconclusive.

An optical charge transfer process between iron and titanium is understood to be the origin of colour in blue sapphire. The overlap of metal d-orbitals of the neighbouring metals facilitates the transfer of an electron between species.[32] The transfer is initiated by visible light absorption, resulting in the alternate valence states of the metals.

$$Fe_{Al}^{\times} + Ti_{Al}^{\times} \xrightarrow{h\nu} Fe_{Al}' + Ti_{Al}^{\bullet} \quad (8)$$

Multiple studies have demonstrated the ease of incorporating Fe and Ti into sapphire and its epitaxial growth for functional applications and analysis.[33–36] As a consequence of heating, the blue colour of a sapphire crystal intensifies, making this a standard industrial process to increase their market value.[27]

In this paper, following our initial communication,[37] we report the calculated optical transition energies of Fe and Ti in the Al_2O_3 lattice and offer suggestions as to the assigning of the absorption spectra of natural sapphires. Our predictions are compared to available experimental evidence. The investigation includes isolated titanium and iron substitutions, the co-doped systems with both metals present in differing valence states, and metal tri-clusters that may form in the lattice.

2 Methodology

We employ Mott-Littleton defect calculations, based on analytical pairwise potentials, to probe the potential energy landscape associated with inter-atomic charge transfer and intra-atomic

crystal field excitations. Further electronic structure calculations are performed using a range of density functionals in order to confirm the ground-state magnetic structures.

2.1 Interatomic potentials

Calculations within the Born model of ionic solids were performed using the GULP (General Utility Lattice Programme) code.[38] The interatomic interactions are represented in the form of the pairwise Buckingham potential, inclusive of a long-range Coulombic term (eqn (9)) evaluated *via* an Ewald summation and a short-range potential active within 15 Å.[39–41] The potential parameters (A, ρ and C) have been taken from Catlow and Lewis to model the pure and doped systems (Table 1).[40,41] The shell model of Dick and Overhauser has been employed to model the electronic polarisation of the system,[42] with the harmonic spring constant (k) fitted to reproduce the experimental high-frequency (ε_∞) and static (ε_0) dielectric tensors. It should be noted that the relatively large error in the calculated elastic constants is common in pair potential methods and does not influence the properties of interest (Table 2).

$$V_{ij} = \frac{q_i q_j}{r_{ij}} + A \exp\left(\frac{r_{ij}}{\rho}\right) - \frac{C}{r_{ij}^6} \quad (9)$$

2.2 Embedded crystal defect calculations

The defect formation energies were calculated within the Mott-Littleton approach.[44] The simulated lattice surrounding the central defect is divided into multiple regions, the details of which have been reviewed extensively elsewhere.[5] Sizes were set at 10 Å (950 ions) and 25 Å (14 278 ions) for regions 1 and 2, respectively. The interatomic potentials used to model the extrinsic transition metals are listed in Table 3.

Two local minimisation approaches were required for the calculation of the energies associated with intervalence charge transfer. The first, full optimisation, results in the lowest energy local configuration of the ions and shells in region 1, calculated *via* a Newton–Raphson procedure. The second minimisation technique is 'shell only'. During this optimisation, the cores of the ions are fixed in location and only the shells are allowed to relax, representing the polarisation of the electrons due to the charge transfer process. As a consequence, a vertical optical transition as defined by the Franck–Condon principle can be modelled, in addition to the adiabatic (thermal) excitation energy. The pairs of ions involved in the intervalence charge transfer (Fe^{II}/Ti^{IV} and Fe^{III}/Ti^{III}), which are charge compensating when substituted into corundum, were modelled separately.

A configurational coordinate diagram can be constructed using the results of the two energy minimisation techniques, as illustrated in Fig. 2. The diagram is a representation of the relative potential energy of different ionic configurations as a function of the defect geometry; the structure of the system is

Table 1 Interatomic potentials used to model corundum as parameterised by Lewis and Catlow[40,41]

Parameter	α – Al_2O_3
A (+ −) (eV)	1474.4
ρ (+ −) (Å)	0.00
C_6 (+ −) (eV Å^6)	0.300
A (− −) (eV)	22 764.3
ρ (− −) (Å)	20.37
C_6 (− −) (eV Å^6)	0.149
Y_+ ($\lvert e^- \rvert$)	1.458
k_+ (eV Å^{-2})	588.71
Y_- ($\lvert e^- \rvert$)	−3.000
k_- (eV Å^{-2})	69.28

Table 2 Calculated properties (structural, dielectric and elastic) for the rhombohedral primitive unit cell of corundum (experimental values taken from the CRC Handbook)[43]

Property	Experiment	Calculated
Lattice energy (eV)	—	−158.94
a, b, c (Å)	4.76	4.83
α, β, γ (°)	55.17	56.79
$\varepsilon_0{}^{11}$	9.34	9.24
$\varepsilon_0{}^{33}$	11.54	13.94
$\varepsilon_\infty{}^{11}$	3.10	3.11
$\varepsilon_\infty{}^{33}$	3.10	3.13
C_{11} (GPa)	497.4	611.28
C_{12} (GPa)	164.00	297.90
C_{44} (GPa)	147.40	134.99

Table 3 Interatomic potentials used to model 3*d* metals in corundum[45]

Parameter	Ti^{III}	Ti^{IV}	Fe^{II}	Fe^{III}
A (+ −) (eV)	1715.7	754.2	694.1	1102.4
ρ (+ −) (Å)	0.0	0.0	0.0	0.0
C_6 (+ −) (eV Å^6)	0.3069	0.3879	0.3399	0.3299
Y_+ ($\lvert e^- \rvert$)	1.23	2.89	2.00	4.97
k_+ (eV Å^{-2})	43.97	37.30	10.92	304.70

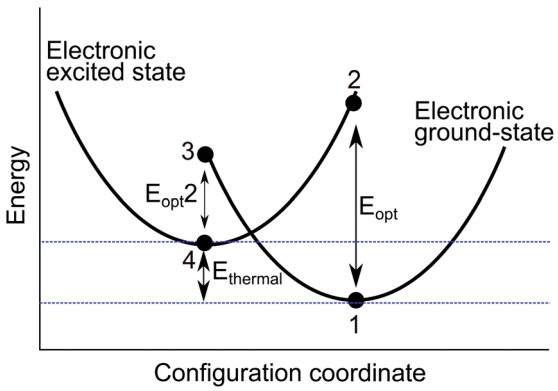

Fig. 2 Configuration coordinate diagram used to illustrate the charge transfer process between two neighbouring cations in the Al_2O_3 structure. It contains both an adiabatic charge transfer energy ($E_{thermal}$), which corresponds to the barrier to thermal activation, and two vertical processes (E_{opt} and $E_{opt}2$). The shape of the curves is schematic.

described by a collective configuration coordinate. Each parabola represents the pair of cations involved in the intervalence charge transfer. The defect energies are labelled 1–4, which have been calculated using the techniques described above. The local minima (1 and 4) are calculated by full geometry optimisation of each charge state. The adiabatic energy E_{thermal} is the difference between these minima. The alternate valence pair is then substituted into the previously optimised positions to model vertical optical excitations (2 and 3).

The calculation of the absolute charge transfer energy between iron and titanium requires an additional term to align their ionisation potentials (E_{diff}), as determined from the lattice energies (ΔE_{LE}) of the respective binary oxides:

$$E_{\text{diff}} = \Delta E_{\text{LE}}\left(\frac{1}{2}(\text{Ti}_2\text{O}_3 + \text{Fe}_2\text{O}_3) - (\text{TiO}_2 + \text{FeO})\right) \quad (10)$$

An alignment term is not required for homonuclear intervalence charge transfer as the ionisation potentials and electron affinity of the two valence states cancel out.

2.3 Ligand field splitting

The AOLM (angular overlap model) developed and implemented by Woodley was employed to obtain the crystal field parameters of the transition metal cations.[46] The inclusion of angular functions into the purely radial Buckingham and Coulomb potentials allows non-spherical cations to be modelled and additional electronic properties to be calculated. The model has been successfully applied to metal oxide structures such as $LaMnO_3$ and Mn_2O_3 which contain non-spherical ions.[47–49] The augmented short-range potentials have been applied to 3d impurities to calculate the energies of the d-orbitals in the distorted environments of the sapphire lattice.

The distortion of the cation environments in sapphire from perfect octahedra, as shown in Fig. 1, reflects their anti-prismatic geometry. In this geometry the octahedral units rotate from the *c*-axis. The pairwise elongation of the oxide ligands results in a pinching and consequent destabilisation of the d_{xy} orbitals. In this configuration the d_{z^2} and $d_{x^2-y^2}$ orbitals are degenerate (Fig. 3).

The crystal field parameters were fitted through the calculations of hexa–aqua complexes in order to obtain the absolute energy splittings for each cation. The interatomic potentials (Table 1 and 3) were used to model these complexes, with the splittings compared to available reference values.[50] Spin–orbit coupling and Jahn–Teller distortions are not considered in this study; however, their effects should be minor. In particular, Jahn-Teller effects will not change the vertical excitation energies.

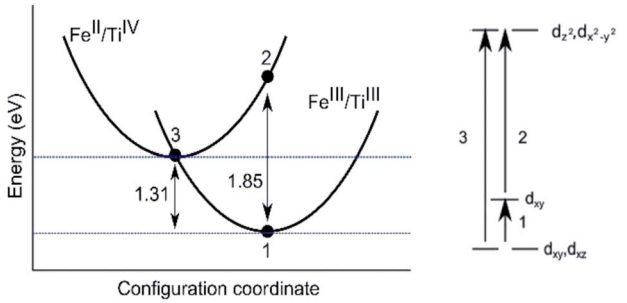

Fig. 3 Configuration coordinate diagram for the intervalence charge transfer between face-sharing iron and titanium bi-particles in the corundum structure (left). The curvature is schematic. An intravalence crystal field diagram of transition metal impurities in sapphire (D_{3d}) symmetry is also drawn (right).

2.4 Electronic structure calculations

To compare with and validate the results obtained using the analytical potentials, first-principles electronic structure calculations were performed on Al_2O_3 using VASP (*Vienna ab initio* Simulation Package).[51–54] Calculations were initially performed by treating the exchange and correlation effects within Density Functional Theory (DFT)[55–57] using the PBEsol generalised gradient functional and a $2 \times 2 \times 2$ *k*-point grid for the supercell. A quasi-Newton relaxation was performed for local structure optimisation, which was converged the forces to 0.005 eV Å^{-1} or lower. The wave functions were constructed *via* a plane wave basis set, with a cut off of 500 eV. The projector augmented wave method was employed to represent the interactions between the core and valence electrons of the ions.[53]

It should be noted that even within an excited-state approach such as time-dependent DFT, the description of charge-transfer

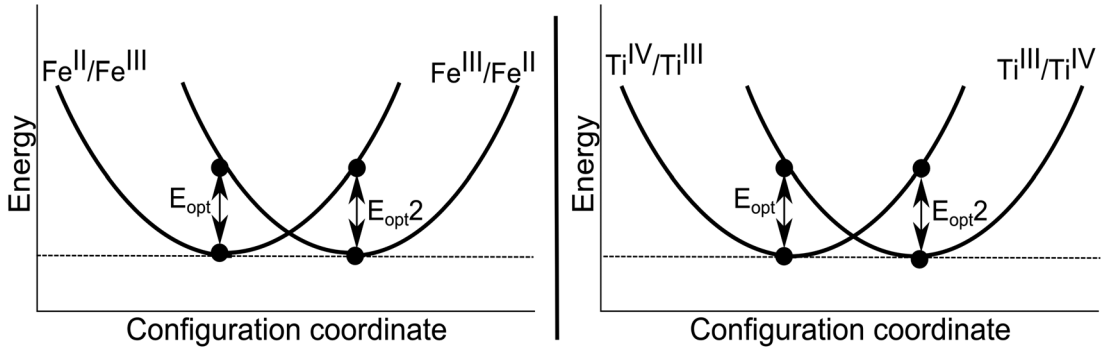

Fig. 4 Schematic configuration coordinate diagrams for the homonuclear charge transfers between face-sharing iron (left) and titanium (right) bi-particles in the corundum structure. Note that the thermal ionisation energy is zero and $E_{\text{opt}} = E_{\text{opt}}2$ by symmetry.

excitations remains a significant challenge. Therefore, the focus of the electronic structure studies here is to probe the ground-state electron and spin distributions. To determine the dependence of the results on the exchange-correlation functional, in particular for the correct magnetic ground state, additional calculations were performed at the DFT + U (5 eV for Ti and Fe d bands), meta-GGA (TPSS and MBJ), hybrid DFT (HSE06) with 25% non-local Fock exchange, and Hartree–Fock (HF) levels of theory.[58–60] Images of chemical structures and electron densities were made using the VESTA software.[61]

We employ the standard supercell approach to investigate Ti and Fe incorporation into Al_2O_3. The conversion from the hexagonal unit cell to an orthorhombic supercell expansion reduces the interactions between defect species in neighbouring supercells.[62] The resulting cuboid was of dimensions 8.27 × 9.55 × 13.01 Å and contained 120 atoms. This was formed by *via* an anisotropic expansion of the form:[63]

$$\begin{pmatrix} 2 & 0 & 0 \\ 1 & 2 & 0 \\ 0 & 0 & 1 \end{pmatrix}$$

For these calculations we have maintained the equilibrium lattice parameters of Al_2O_3, relaxing only the internal coordinates during the defect calculations, which is appropriate for perturbations in the dilute limit. Effective doping concentrations for the singularly and co-doped systems were 0.83% and 1.67%, respectively.

3 Results and discussion

3.1 Ti-doped sapphire

Sapphires doped only with Ti in the trivalent state are pale pink in colour representing the absorption of energy between 2.21 and 2.53 eV, as confirmed by optical spectroscopy. More specifically, absorption maxima are given as 2.25 eV and 2.56 eV by Johnson *et al.*[64] As shown in Table 4 our calculated crystal field parameter of 2.47 eV is in good agreement.[65] The three underlying optical processes are labelled in Fig. 3.

With a 13% increase in ionic radius, Ti^{III} incorporation causes a distortion to the local structure. Bond lengths for the face and edge-sharing configurations are 2.81 Å and 2.90 Å, respectively. We have calculated the solutional substitutional enthalpy of each metal dopant in the sapphire lattice, representing the incorporated isolated defect at infinite dilution (see eqn (1)–(6)). This enthalpy was calculated by the subtraction of the total energy of the defective system (with the dopant present) from that of the pure system (with no defects present), which was balanced thermodynamically using the lattice energies of the binary oxides of the 3d metal dopants (eqn (1)).

In addition to a substitution energy of 3.41 eV, we have found that isovalent titanium disrupts the local environment around the lattice site. However, the cations remain in a trigonal antiprismatic geometry (Fig. 1). Typical intensities of d–d transitions range between 1–10^3 M^{-1} cm^{-1} (Table 5), but due to the distortion of the 3d cations the intensities of these transitions should be greater. The solutional substitution energy for the optically inactive Ti^{IV} is calculated to be 2.78 eV and 3.05 eV from eqn (2) and (3), respectively.

3.2 Fe-doped sapphire

Fe is found in sapphires in both its divalent and trivalent oxidation states.[36,67] Sapphires doped only with Fe, predominately in the trivalent state, are yellow in colour. It is still under debate if this is due to intravalence d–d transitions within a single impurity, or to an intervalence charge transfer between the divalent and trivalent valences of iron.[26,31,68] This colour arises from visible light absorption in the energy region of between 2.88 eV and 3.26 eV.

The energy calculated for the intra-valence transition in trivalent Fe is 2.94 eV (Table 4), which is within the measured energy range.[26] The results suggest, in support of Ferguson and Fielding, that visible light absorption in Fe-doped sapphire is due to intra-valence d–d transitions in the dopant cation even though all electronic transitions in these dopants are formally spin forbidden. Typical intensities for such transitions are given in Table 5. As shown they range between 10^{-5}–10^0 M^{-1} cm^{-1}. The electron transfer energy between divalent and trivalent Fe has also been calculated to further support this conclusion (see Section 3.3).

The calculated enthalpy of solution for Fe^{III} (eqn (4)) is 0.40 eV, while for Fe^{II} the two compensation mechanisms (eqn (5) and (6)) were calculated to be 1.12 eV and 1.53 eV, respectively. The larger ionic radii of Fe^{II} and Fe^{III} in comparison to Al^{III} is 7% and 1%, respectively, which contributes to the smaller solution energy of the latter. The isovalent Fe^{III} substitution also avoids the formation of charge compensating point defects. When considering the difference in enthalpy of solution for isolvalent Ti and Fe, the increased energy calculated for Ti is purely due to the steric affect of the size of either cation. As Ti is larger than Fe the distortion of the lattice with its substitution is greater, which has an associated energetic penalty.

Table 4 Calculated crystal field transition energies (in eV) for isolated Ti^{III} (d^1) and Fe^{III} (d^5) impurities in the corundum structure. 1, 2 and 3 refer to the first three optical transitions for D_{3d} symmetry (see Fig. 3), while (SF) denotes a spin forbidden transition

Optical transition			
	1	2	3
Ti	0.28	2.19	2.47
Fe	0.90 (SF)	2.14 (SF)	2.94 (SF)

Table 5 Typical absorption intensities for optical processes as governed by the given selection rules[66]

Governing condition	Range of absorption intensities (ε) (M^{-1} cm^{-1})
Spin and symmetry forbidden	10^{-5}–10^0
Spin-allowed, symmetry-forbidden	10^0–10^3
Spin and symmetry allowed	10^3–10^5

3.3 Co-doping sapphire

3.3.1 Fe/Ti: ionic potentials. Experimental evidence for the presence of bi-particles (neighbouring substitutional impurities) in sapphire was first reported by Eigenmann (1972) and has since been of great interest as to the effect on pleochroism and the colour of materials.[30,69] When neighbouring in the corundum structure an overlap of the metal d-orbitals, *i.e.* d_{z^2} and $d_{x^2-y^2}$, facilitates the efficient transfer of an electron between the cations. We have shown that the Fe^{III} and Ti^{III} charge states are thermodynamically favored for the isolated ions; we have also calculated that this is true for co-doping.

When neighbouring, Fe^{III} and Ti^{III} are at a distance ranging from 2.88 to 2.99 Å. An electron can be transferred between the species, initiated by the absorption of light, resulting in the Fe^{II}/Ti^{IV} configurations being formed (eqn (8)). This intervalence charge transfer is not limited by symmetry or spin selection rules, resulting in optically allowed transitions.

The energy absorbed during the intervalence optical transfer has been speculated to be responsible for the intense blue colour of sapphire, with this initial suggestion dating back to 1967.[31] Alternative mechanisms are still debated, *e.g.* that Ti is a charge compensating cation and Fe is the colour centre.[28] However, it is more popularly considered that the Fe^{II}/Ti^{IV} configuration represents the ground state and Fe^{III}/Ti^{III} the excited state.[26,29,69,70] We confirm that intervalence charge transfer is responsible for colour, but this instead occurs for the Fe^{III}/Ti^{III} pairs.[37] For this to be a viable mechanism, an energy between 1.99 and 2.14 eV must be absorbed.

We have calculated the energy required for the transfer of an electron between Fe^{III} and Ti^{III} (the principal absorption) in both edge and face-sharing configurations. There is a third possible environment where the cations could be substituted parallel to the *c*-axis, resulting in a separation of 3.37 Å. The transfer of an electron would be less probable, due to smaller d-orbital overlap and substitution at this site has therefore not been investigated. As shown in Fig. 3, the absorption occurs with the transfer of an electron from the more stable Fe^{III}/Ti^{III} to Fe^{II}/Ti^{IV}. The Fe^{II}/Ti^{IV} configuration represents a metastable excited state; thermal relaxation (1.31 eV) to the Fe^{III}/Ti^{III} configuration is favoured; however, we cannot comment on the timescale for this process.[37]

We have also investigated the energy associated with defect clustering. For the Fe^{II}/Ti^{IV} configuration there is a binding energy of 0.64 eV owing to the strong Coulomb attraction of oppositely charge defects, which may stabilise neighbouring impurities during synthesis or annealing:

$$Fe'_{Al} + Ti^{\bullet}_{Al} \rightarrow [Fe_{Al} + Ti_{Al}]^{\times} \quad (11)$$

Absorption spectroscopy shows a strong, broad band with maximum between 2.14 and 2.17 eV.[29,70] We can assign this peak as the intervalence charge transfer for the co-doped systems between Ti^{III} and Fe^{III} (eqn (8)). The measured signal is broadened by the changes in environment that are characteristic of an intervalence charge transfer.

3.3.2 Fe/Ti: electronic structure. Due to the importance of the "blue" transition and the assignment of the ground state Ti/Fe configuration, further calculations were carried out based on spin DFT to ensure that the correct ground-state had been identified.

Firstly the corundum structure was optimised (PBEsol functional), with good agreement with both experiment and the pair potentials.[51–54] The dopants were then incorporated in adjacent sites for the substitution of Al in both orientations, as had previously been modelled with the ionic potentials. The relative energies were assessed based on the self-consistent total energies.

Different magnetic and charge-state configurations can be stabilised accordingly to the initialisation of the calculation in terms of total and local magnetic moments. Spin density profiles ($\rho^{\uparrow} - \rho^{\downarrow}$) were plotted to confirm the location and topology of the magnetisation. These results were compared to the configurational coordinate diagram (Fig. 2). The d occupations associated with each of the metals in their formal oxidation states are $d^0(Ti^{IV})$, $d^1(Ti^{III})$, $d^5(Fe^{III})$ and $d^6(Fe^{II})$. For Ti, the local spin moment is well defined; however, Fe may access both low (LS) and high (HS) spin configurations. In the binary oxide FeO, Fe^{II} adopts a high spin configuration (with anti-ferromagnetic alignment), while in haematite, corundum structured Fe_2O_3, Fe^{III} is also high spin (with anti-ferromagnetic alignment).[71–73]

As shown by the spin-density profiles, independent of the magnetic initialisation, when the metals were in high spin, the Fe^{II}/Ti^{III} configuration was always observed (Table 7). This phenomenon confirms the instability of the Fe^{II}/Ti^{IV} configuration and supports the configurational coordinate diagram. This spontaneous electron transfer demonstrates that the Fe^{II}/Ti^{IV} configuration is less stable, in agreement with the pair potential results. Calculations based upon hybrid and meta-DFT, as well as HF, confirm the absence of electron transfer (Table 7).

The energies of all configurations relative to the calculated ground-state high spin Fe^{III}/Ti^{III} are presented in Table 7. In low spin, when the Fe^{II}/Ti^{IV} pair is stabilised, the resultant configuration is 1.18 eV higher than the ground-state. The energy difference between the two optimised configurations (1.18 eV) also closely correlates to the adiabatic electron transfer reported in the previous section (1.31 eV). We note

Table 6 Intervalence charge transfer energies (vertical optical transitions) between substitutional bi-particles in the corundum structure. UNS refers to a configuration unstable with respect to optimisation

Bi-particle	Configuration	Process	Energy (eV)
Fe^{III}/Ti^{III}	Face-sharing	E_{opt}	1.85
Fe^{II}/Ti^{IV}	Face-sharing	$E_{opt}2$	0.00
Fe^{III}/Ti^{III}	Edge-sharing	E_{opt}	1.76
Fe^{II}/Ti^{IV}	Edge-sharing	$E_{opt}2$	UNS
Fe^{II}/Fe^{III}	Face-sharing	E_{opt}	1.43
Fe^{II}/Fe^{III}	Edge-sharing	E_{opt}	1.30
Ti^{III}/Ti^{IV}	Face-sharing	E_{opt}	1.44
Ti^{III}/Ti^{IV}	Edge-sharing	E_{opt}	UNS

Table 7 Self-consistent spin density profiles from electronic structure calculations for the Fe/Ti co-doped sapphire. Neighbouring Ti (left) and Fe (right). Spin (S) refers to the total spin moment that was fixed for the supercell, LS indicates a low spin configuration for Fe, while *E* refers to the total energy of the supercell relative to the most stable configuration. Positive spin density (yellow) and negative spin density (blue) are shown for an isolated fragment of the periodic supercell. The same spin topology and energetic ordering was found for meta-GGA and DFT + U functionals (not shown)

Theory	*S*	Initialisation	Output	*E* (eV)	Spin density
HSE06	(4/2)	$Ti^{IV(d^0)}/Fe^{II(d^6)}$	$Ti^{III\downarrow}/Fe^{III}$	0.00	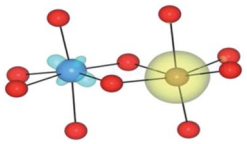
HSE06	(6/2)	$Ti^{III(d^1)}/Fe^{III(d^5)}$	$Ti^{III\uparrow}/Fe^{III}$	0.82	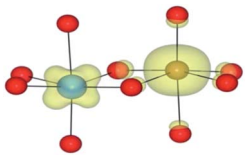
HSE06	(4/2)	$Ti^{III(d^1)}/Fe^{III(d^5)}$	$Ti^{III\downarrow}/Fe^{III}$	0.04	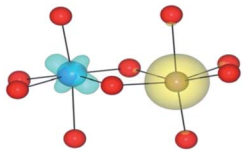
HSE06	(0/2)	$Ti^{IV(d^0)}/Fe^{II(d^6)(LS)}$	Ti^{IV}/Fe^{II}	1.18	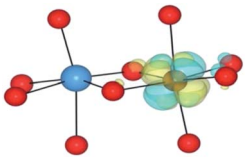
HSE06	(2/2)	$Ti^{III(d^1)}/Fe^{III(d^5)(LS)}$	$Ti^{III\uparrow}/Fe^{III}$	1.30	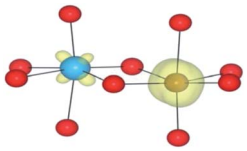
HSE06	(0/2)	$Ti^{III(d^1)}/Fe^{III(d^5)(LS)}$	Ti^{IV}/Fe^{II}	1.18	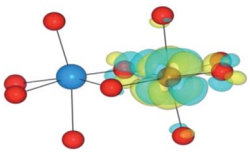
HF	(4/2)	$Ti^{IV(d^0)}/Fe^{II(d^6)}$	$Ti^{III\downarrow}/Fe^{III}$	—	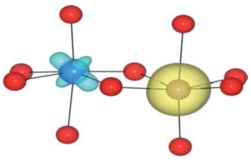

that in order to fully probe the optical excitations from electronic structure theory, an explicit time dependent approach should be applied.

Table 8 Binding energies of bi-particles (per pair) in the sapphire lattice. Negative values refer to exothermic binding

Bi-particle	Binding energy (eV)
Fe^{III}–Ti^{III}	−0.02
Fe^{II}–Ti^{IV}	−0.64
Fe^{II}–Fe^{III}	0.00
Ti^{III}–Ti^{IV}	−0.02

3.3.3 Fe/Fe and Ti/Ti aggregates. The energies associated with homonuclear Fe and Ti impurity pairs have been calculated using the ionic potentials, DFT and HF methods. The ionic potentials were employed to obtain the intervalence charge transfer energies, while the electronic structure approaches were used to probe the local spin configurations.

Both Fe^{III}/Fe^{II} and Ti^{III}/Ti^{IV} pairs were considered. The calculated charge transfer energies are given in Table 6. The energy of homonuclear intervalence charge transfer has been calculated to occur in the thermal range. These have no direct contribution to the colour of the crystal, but will influence the thermoelastic properties.

The mirror symmetry of the transitions (E_{opt} and E_{opt}^2) are typical of a homonuclear system, with each configuration representing the same valence states of cations but occupying the opposite sites in the lattice. From these calculated results of 1.2–1.4 eV, we can further conclude the origin of the colour of yellow sapphires to be due to the intra-valence transitions in the Fe^{III} cations (Table 4) and not due to homonuclear intervalence charge transfer (Table 6).

Binding energies of 0.00 eV and −0.02 eV were calculated for Fe^{II}/Fe^{III} and Ti^{III}/Ti^{IV} pairs with bond lengths of 2.92 Å and 3.05 Å, respectively. Results suggest that there is no strong driving force for impurity aggregation and hence a low probability of homonuclear charge transfer.

We have also performed electronic structure analysis of the homonuclear systems for neighbouring aliovalent pairs. Spin density profiles have been plotted to illustrate the magnetic structure and are presented in Table 9. The limitations of the underlying DFT and HF techniques should be noted, which are based on a single determinant when calculating the self-consistent field, which means that the electronic minimisation procedure is unable to distinguish between symmetric homonuclear cations. As a consequence, the models may be biased towards electron delocalisation between the two metal centres.

For the homonuclear Fe system, the spin density is similar – and almost spherical – on each ion. Results are shown for the most stable high-spin configuration, which suggests a preference for two $Fe^{III}(d^5)$ ions with the occupation of the minority spin t_{2g} orbital split between them. An equivalent electron count is found around each metal. The same results were observed at the GGA, hybrid DFT and HF levels of theory; the latter two results are shown in Table 9. Results including explicit breaking of the homonuclear symmetry are also presented. A model isoelectronic heteronuclear system was constructed: Co^{III}/Fe^{III}, *i.e.* d^6/d^5. As shown, the topology of the Co/Fe spin density is similar, but analysis of electronic charge and magnetisation for each ions confirms the occupation of the minority spin t_{2g} state on Co. Therefore, neighbouring d^6/d^5 centres are possible.

Analysis of the spin density for the homonuclear Ti system displays a similar delocalisation when modelled at all levels of theory (Table 9). Instead of a d^1/d^0 configuration, a single d band on each Ti centre is partially occupied by one electron. Within HF theory, which fully describes the electron-exchange term, the density is also depicted as delocalised (positive spin density on both Ti cations), suggesting this effect is not due to the electron self-interaction, which was further confirmed using the electron localisation function.[74,75] A model calculation was again conducted to remove the mirror symmetry, *via* the substitution of one Ti for Y: Ti^{III}/Y^{III}, *i.e.* d^1/d^0. Here, the single d electron is forced to localise on Ti, resulting in the asymmetric spin density shown in Table 9. These results confirm that neighbouring d^1/d^0 centres are also possible, but appear not to be accessible for the homonuclear system, at least not within a single-determinant framework.

Table 9 Self-consistent spin density profiles (yellow isosurface) from calculations for $(Fe/Fe)^-$ and $(Ti/Ti)^+$ doped sapphire. The systems (Co/Fe) and (Y/Ti) were also investigated as isoelectronic analogues. The spin (*S*) refers to the total spin moment fixed for the supercell

Theory	*S*	Initialisation	Spin density
HSE06	(9/2)	$Fe^{III(d^5)}/Fe^{II(d^6)}$	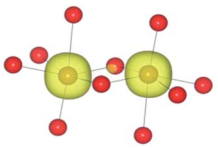
HF	(9/2)	$Fe^{III(d^5)}/Fe^{II(d^6)}$	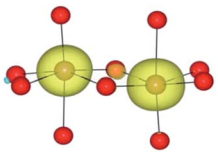
HSE06	(9/2)	$Co^{III(d^6)}/Fe^{III(d^5)}$	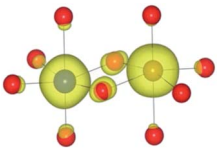
HSE06	(1/2)	$Ti^{III(d^1)}/Ti^{IV(d^0)}$	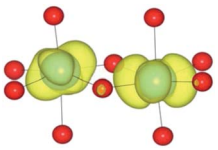
HF	(1/2)	$Ti^{III(d^1)}/Ti^{IV(d^0)}$	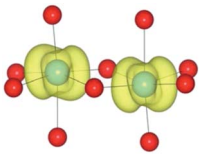
HSE06	(1/2)	$Y^{III(d^0)}/Ti^{III(d^1)}$	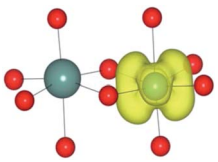

3.4 Tri-clusters in sapphire

In addition to isolated defects and bi-particles, larger defect clusters are also possible, especially at high impurity concentrations. The attraction and consequent binding of charge compensating defects, with the substitution of Al for an aliovalent cation has previously been reported.[23,76]

We have modelled possible metal tri-clusters to assess their optical properties and to see if they can further stabilise Fe^{II}/Ti^{IV} pairs (Table 10). All tri-clusters have been modelled as L-shaped, with each cluster containing edge and face-sharing metals (Fig. 5). The co-doped edge-sharing Fe^{II}/Ti^{IV} configurations were unstable, this is also true when incorporated into a tri-cluster configuration. We therefore modelled the tri-clusters involving Fe^{II}/Ti^{IV} as face-sharing, with the third metal in an edge-sharing configuration.

The calculations demonstrate that the intervalence charge transfer energy between trivalent Fe and Ti remains within the visible range when present in a tri-cluster. Absorption energies remain almost unchanged compared to the isolated pairs. There is only one cluster, $[Ti^{III}–(Ti^{IV}–Fe^{II})]$, which gains stability by forming this aggregate (Table 8). It is unlikely that the remaining clusters would form to any significant concentration.

Table 10 Binding energy and charge transfer energy (in eV) for the most stable metal tri-clusters calculated using interatomic potentials. Metals in parentheses are parallel to the central metal in the cluster

Cluster	Binding	E_{opt}^{Fe-Ti}
Fe^{III}–(Ti^{III}–Fe^{III})	−0.13	1.84
Fe^{III}–(Fe^{III}–Ti^{III})	−0.15	1.91
Fe^{III}–(Ti^{IV}–Fe^{II})	−0.33	−0.05
Fe^{III}–(Fe^{II}–Ti^{IV})	−0.44	0.17
Ti^{III}–(Ti^{IV}–Fe^{II})	−0.89	−0.09

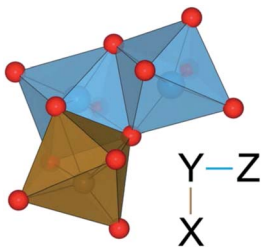

Fig. 5 Illustration of a Ti^{III}–(Ti^{IV}–Fe^{II}) tri-cluster. The L-shaped geometry of metal tri-clusters is shown, where *X*–*Y* are edge-sharing and *Y*–*Z* are face-sharing. The notation *X*–(*Y*–*Z*) is used in Table 10.

The [Ti^{III}–(Ti^{IV}–Fe^{II})] cluster would offer a greater stability to the Fe^{II}/Ti^{IV} pairs and may extend their lifetime in the crystal. However, even if formed, the optical process would remain largely unchanged by the third neighbouring cation. We propose that experimental detection of these aliovalent cations can be due either to the isolated Ti^{IV}–Fe^{II} pairs, or their presence within the tri-cluster as described. Homonuclear intervalence charge transfer was also modelled in these tri-clusters and the energies were found to remain unaffected (Table 10).

Preliminary attempts to model more complex clusters consisting of these metal dopants with charge compensating intrinsic point defects such as vacancies and interstitials have been made. However, these larger clusters have large positive binding energies and therefore will not form under conditions of thermodynamic equilibrium in sapphire.

4 Conclusions

We have investigated the structural, energetic and optical properties of Ti and Fe in the corundum Al_2O_3 lattice using two materials modelling techniques. Our insights can be summarised as follows:

1. Crystal field parameters have been calculated for the trivalent cations showing their intra-valence optical transitions to occur within the visible light region.

2. The dominant intervalence charge transfer resulting in the absorption of visible light occurs between Fe^{III}/Ti^{III} to produce the metastable Fe^{II}/Ti^{IV} configuration.

3. Electronic structure calculations have confirmed the instability of the Fe^{II}/Ti^{IV} pairs in sapphire, with total energies more than 1 eV higher than the Fe^{III}/Ti^{III} configuration.

4. Homonuclear iron and titanium charge transfer has been shown to occur within the IR range and will have no contribution to visible light absorption of the material.

5. Electronic structure calculations, based on DFT and HF, have been unable to stabilise nearest neighbour Fe^{II}/Fe^{III} and Ti^{III}/Ti^{IV} pairs. Delocalisation of the excess electron occurs between the two metal centres, which would prohibit nearest-neighbour intra-valence charge transfer.

6. Possible Ti and Fe tri-clusters in differing nearest neighbour configurations were modelled. The calculated binding energies between these species identified one configuration to be thermodynamically accessible. [Ti^{III}–(Ti^{IV}–Fe^{II})] is the most stable combination, which may be formed in doped sapphire samples.

Moving beyond low concentrations of defects, ternary and quaternary compounds formed of these elements should display a similar behaviour. Ilmenite ($FeTiO_3$) also adopts the corundum structure, consisting of edge and face-sharing iron and titanium cations throughout the crystal structure.[77,78] A description of charge transfer processes in these systems, within a first-principles framework, would represent a major development to their materials chemistry.

Acknowledgements

J.K.B is funded by the EPSRC (Grant no. EP/G03768X/1). We would like to thank C.R.A. Catlow and S.M. Woodley for useful discussions and use of the AOLM. A.W. acknowledges support from the Royal Society University Research Fellowship scheme. D.T. was funded under ERC Starting Grant 277757. The work benefits from the high performance computing facility at the University of Bath. Access to the HECToR supercomputer was facilitated through membership of the HPC Materials Chemistry Consortium (EP/F067496).

References

1 K. Wall and A. Sanchez, *Linc. Lab. J.*, 1990, **3**, 447–462.
2 A. K. Datye, *J. Catal.*, 2003, **216**, 144–154.
3 D. Redfield, *Appl. Phys. Lett.*, 1974, **25**, 647–648.
4 P. W. M. Jacobs and E. A. Kotomin, *Philos. Mag.*, 1993, **68**, 695–709.
5 C. R. A. Catlow, R. James, W. C. Mackrodt and R. F. Stewart, *Phys. Rev. B: Condens. Matter Mater. Phys.*, 1982, **25**, 1006–1026.
6 D. McClure, *J. Chem. Phys.*, 1962, **36**, 2757.
7 Y. Kitaoka, K. Nakamura, T. Akiyama, T. Ito, M. Weinert and A. Freeman, *Phys. Rev. B: Condens. Matter Mater. Phys.*, 2013, **87**, 205113.
8 M. Choi, A. Janotti and C. G. Van de Walle, *J. Appl. Phys.*, 2013, **113**, 044501–044505.
9 N. Hine, P. Haynes, A. Mostofi and M. Payne, *J. Chem. Phys.*, 2010, **133**, 114111–114123.
10 W. H. Bragg, *J. Am. Chem. Soc.*, 1922, **121**, 2766–2787.
11 S. Mitra, *Fundamentals of Optical, Spectroscopic and X-ray Mineralogy*, New Age International, 1996.
12 K. S. Jheeta and D. C. Jain, *Afr. Phys. Rev.*, 2008, **1**, 56–66.

13 L. Cuadra, A. Martí and A. Luque, *IEEE Trans. Electron Devices*, 2004, **51**, 1002–1007.
14 S. Licht, *J. Phys. Chem. B*, 2001, **105**, 6281–6294.
15 J. Baltrusaitis, C. D. Hatch and R. Orlando, *J. Phys. Chem. C*, 2012, **116**, 18847–18856.
16 Y. Ikuma and R. S. Gordon, *J. Am. Ceram. Soc.*, 1983, **66**, 139–147.
17 A. R. Moon and M. R. Phillips, *J. Am. Ceram. Soc.*, 1994, **77**, 356–367.
18 J. Zhang, J. Ding and Y. Zhang, *Solid State Commun.*, 2009, **149**, 1188–1192.
19 P. Lacovara, L. Esterowitz and M. Kokta, *IEEE J. Quantum Electron.*, 1985, **21**, 1614–1618.
20 F. Seifert, V. Petrov and M. Woerner, *Opt. Lett.*, 1994, **19**, 2009–2011.
21 P. F. Moulton, *et al.*, *Opt. News*, 1982, **8**, 9.
22 J. M. Eggleston, L. G. Deshazer and K. W. Kangas, *IEEE J. Quantum Electron.*, 1988, **24**, 1009–1015.
23 K. J. W. Atkinson, R. W. Grimes, M. R. Levy, Z. L. Coull and T. English, *J. Eur. Ceram. Soc.*, 2003, **23**, 3059–3070.
24 F. A. Kröger and H. J. Vink, *Solid State Phys.*, 1956, **3**, 307–435.
25 N. Yu, Q. Wen, D. R. Clarke, P. C. McIntyre, H. Kung, M. Nastasi, T. Simpson, I. Mitchell and D. Li, *J. Appl. Phys.*, 1995, **78**, 5412–5421.
26 J. Ferguson and P. E. Fielding, *Aust. J. Chem.*, 1972, **25**, 1371–1385.
27 T. Kittiauchawal and P. Limsuwan, *Kasetsart J.*, 2007, **41**, 262–266.
28 G. Lehmann and H. Harder, *Am. Mineral.*, 1970, **55**, 98–105.
29 L. V. Nikolskaya, V. M. Terekhova and M. I. Samoilovich, *Phys. Chem. Miner.*, 1978, **3**, 213–224.
30 M. N. Taran and M. Koch-Müller, *Phys. Chem. Miner.*, 2011, **38**, 215–222.
31 M. G. Townsend, *Solid State Commun.*, 1968, **6**, 81–83.
32 R. G. Burns, *Mineralogical Applications of Crystal Field Theory*, Cambridge University Press, 1993, vol. 5.
33 G. W. Hollenberg and R. S. Gordon, *J. Am. Ceram. Soc.*, 1973, **56**, 140–147.
34 E. Traversa, M. Baroncini, E. Di Bartolomeo, G. Gusmano, P. Innocenzi, A. Martucci and A. Bearzotti, *J. Eur. Ceram. Soc.*, 1999, **19**, 753–758.
35 J. Tartaj and G. L. Messing, *J. Eur. Ceram. Soc.*, 1997, **17**, 719–725.
36 N. Yu and M. Nastasi, *Appl. Phys. Lett.*, 1994, **65**, 180–182.
37 J. K. Bristow, S. C. Parker, C. R. A. Catlow, S. M. Woodley and A. Walsh, *Chem. Commun.*, 2013, **49**, 5259–5261.
38 J. D. Gale, *J. Chem. Soc., Faraday Trans.*, 1997, **93**, 629–637.
39 P. P. Ewald, *Ann. Phys.*, 1921, **64**, 253.
40 C. R. A. Catlow, *Proc. R. Soc. A*, 1977, **353**, 533–561.
41 G. V. Lewis, *Physica B + C*, 1985, **131**, 114–118.
42 B. G. Dick and A. W. Overhauser, *Phys. Rev.*, 1958, **112**, 90.
43 D. R. Lide, *CRC Handbook of Chemistry and Physics*, CRC press, 2012.
44 N. F. Mott and M. J. Littleton, *Trans. Faraday Soc.*, 1938, **34**, 485–499.
45 G. V. Lewis and C. R. A. Catlow, *J. Phys.: Condens. Matter*, 1985, **18**, 1149–1161.
46 S. M. Woodley, P. D. Battle, C. R. A. Catlow and J. D. Gale, *J. Phys. Chem. B*, 2001, **105**, 6824–6830.
47 S. M. Woodley, P. D. Battle, J. D. Gale and C. R. A. Catlow, *Phys. Chem. Chem. Phys.*, 1999, **1**, 2535–2542.
48 S. M. Woodley, C. R. A. Catlow, J. D. Gale and P. D. Battle, *Chem. Commun.*, 2000, 1879–1880.
49 S. M. Woodley, P. D. Battle, J. D. Gale and C. R. A. Catlow, *Chem. Mater.*, 2003, **15**, 1669–1675.
50 J. E. Huheey, E. A. Keiter, R. L. Keiter and O. K. Medhi, *Inorganic chemistry: principles of structure and reactivity*, Harper & Row, New York, 1983, p. 412.
51 G. Kresse and J. Hafner, *Phys. Rev. B: Condens. Matter Mater. Phys.*, 1994, **49**, 14251.
52 G. Kresse and J. Furthmüller, *Comput. Mater. Sci.*, 1996, **6**, 15–50.
53 P. E. Blöchl, *Phys. Rev. B: Condens. Matter Mater. Phys.*, 1994, **50**, 17953.
54 J. P. Perdew, K. Burke and M. Ernzerhof, *Phys. Rev. Lett.*, 1996, **77**, 3865–3868.
55 P. Hohenberg and W. Kohn, *Phys. Rev.*, 1964, **136**, B864.
56 L. Sham and W. Kohn, *Phys. Rev.*, 1966, **145**, 561.
57 J. P. Perdew and A. Zunger, *Phys. Rev. B: Condens. Matter Mater. Phys.*, 1981, **23**, 5048.
58 V. I. Anisimov, F. Aryasetiawan and A. Lichtenstein, *J. Phys.: Condens. Matter*, 1997, **9**, 767.
59 J. Heyd, J. E. Peralta, G. E. Scuseria and R. L. Martin, *J. Chem. Phys.*, 2005, **123**, 174101.
60 J. P. Perdew, S. Kurth, A. Zupan and P. Blaha, *Phys. Rev. Lett.*, 1999, **82**, 2544–2547.
61 K. Momma and F. Izumi, *J. Appl. Crystallogr.*, 2011, **44**, 653–658.
62 A. Walsh, J. L. F. Da Silva, Y. Yan, M. M. Al-Jassim and S. H. Wei, *Phys. Rev. B: Condens. Matter Mater. Phys.*, 2009, **79**, 073105.
63 A. A. Sokol, A. Walsh and C. R. A. Catlow, *Chem. Phys. Lett.*, 2010, **492**, 44–48.
64 M. L. Johnson, M. E. Mercer, E. Fritsch, P. Maddison and J. E. Shigley, *Gems Gemol.*, 1995, **31**, 188–195.
65 P. Lacovara, L. Esterowitz and M. Kokta, *IEEE J. Quantum Electron.*, 1985, **21**, 1614–1618.
66 D. C. Harris and M. D. Bertolucci, *Symmetry and Spectroscopy: an Introduction to Vibrational and Electronic Spectroscopy*, Dover Publications, 1989.
67 N. Udomkan, P. Limsuwan, P. Winotai and S. Meejoo, *Int. J. Mod. Phys. B*, 2005, **19**, 3273–3284.
68 V. Palanza, A. Galli, R. Lorenzi, F. Moretti, M. C. Mozzati, A. Paleari and G. Spinolo, *Luminescence study of transition metal ions in natural magmatic and metamorphic yellow sapphires*, 2010, vol. 15, p. 12086.
69 K. Eigenmann and H. H. Günthard, *Chem. Phys. Lett.*, 1972, **13**, 58–61.
70 I. Fontana, A. Le Donne, V. Palanza, S. Binetti and G. Spinolo, *J. Phys.: Condens. Matter*, 2008, **20**, 125228.
71 I. Dzyaloshinsky, *J. Phys. Chem. Solids*, 1958, **4**, 241–255.
72 J. Badro, V. V. Struzhkin, J. Shu, R. J. Hemley, H.-k. Mao, C.-c. Kao, J.-P. Rueff and G. Shen, *Phys. Rev. Lett.*, 1999, **83**, 4101–4104.

73 I. Solovyev, A. Liechtenstein and K. Terakura, *J. Magn. Magn. Mater.*, 1998, **185**, 118–120.
74 A. D. Becke and K. E. Edgecombe, *J. Chem. Phys.*, 1990, **92**, 5397.
75 A. Savin, O. Jepsen, J. Flad, O. K. Andersen, H. Preuss and H. G. von Schnering, *Angew. Chem., Int. Ed. Engl.*, 1992, **31**, 187–188.
76 K. P. D. Lagerlöf and R. W. Grimes, *Acta Mater.*, 1998, **46**, 5689–5700.
77 N. C. Wilson, J. Muscat, D. Mkhonto, P. E. Ngoepe and N. M. Harrison, *Phys. Rev. B: Condens. Matter Mater. Phys.*, 2005, **71**, 075202.
78 G. R. Seda and T. Hearne, *J. Phys.: Condens. Matter*, 2004, **16**, 2707.